T 1D -weighted ihMT imaging – Part II. Investigating the long- and short-T 1D components correlation with myelin content. Comparison with R 1 and the macromolecular proton fraction

Andreea Hertanu, Lucas Soustelle, Julie Buron, Julie Le Priellec, Myriam Cayre, Arnaud Le Troter, Gopal Varma, David C Alsop, Pascale Durbec, Olivier Girard, et al.

T_{1D}-weighted ihMT imaging – Part II. Investigating the long and short T_{1D} components correlation with myelin content. Comparison with R_1 and the macromolecular proton fraction (MPF).

Andreea Hertanu[1,2], Lucas Soustelle[1,2], Julie Buron[1,2,3], Julie Le Priellec[3], Myriam Cayre[3], Arnaud Le Troter[1,2], Gopal Varma[4], David C. Alsop[4], Pascale Durbec[3], Olivier M. Girard[1,2], Guillaume Duhamel[1,2]*

1. Aix Marseille Univ, CNRS, CRMBM, Marseille, France

2. APHM, Hôpital Universitaire Timone, CEMEREM, Marseille, France

3. Aix Marseille Univ, CNRS, IBDM, Marseille, France

4. Division of MR Research, Radiology, Beth Israel Deaconess Medical Center, Harvard Medical School, Boston, MA, United States

*Corresponding author:

Guillaume Duhamel

Centre de Résonance Magnétique Biologique et Médicale

Aix Marseille University, CNRS UMR 7339

13005 Marseille, France

guillaume.duhamel@univ-amu.fr

+33 491 386 260

ABSTRACT (word count: 239 words)

Purpose: To investigate the long and short T_{1D} components correlation with myelin content using ihMT high-pass and bandpass T_{1D}-filters and to compare ihMT, R_1, and the macromolecular proton fraction (MPF) for myelin specific imaging.

Methods: 3D ihMTRAGE sequences with increasing switching times (Δt) were used to derive ihMT high-pass T_{1D}-filters with increasing T_{1D} cutoff values and an ihMT bandpass T_{1D}-filter for components in the 100 µs to 1 ms range. 3D SPGR-qMT protocols were used to derive R_1 and MPF maps. The specificity of R_1, MPF and ihMT T_{1D}-filters was evaluated by comparison to two histological reference techniques for myelin imaging.

Results: The higher contribution of long T_{1D}s as compared to the short components as Δt got longer led to an increase in the specificity to myelination. In contrast, focusing on the signal originating from a narrow range of short T_{1D}s (< 1 ms) as isolated by the bandpass T_{1D}-filter led to lower specificity. In addition, the significantly lower r^2 correlation coefficient of the bandpass T_{1D}-filter suggests that the origin of short T_{1D} components is mostly associated with non-myelin protons. Also, the important contribution of short T_{1D}s to the estimated MPF, explains its low specificity to myelination as compared to the ihMT high-pass T_{1D}-filters.

Conclusion: Long T_{1D} components imaging by means of ihMT high-pass T_{1D}-filters is proposed as an MRI biomarker for myelin content. Future studies should enable the investigation of the sensitivity of ihMT T_{1D}-filters for demyelinating processes.

Keywords: ihMT T_{1D}-filtering, long T_{1D} components, short T_{1D} components, myelin specificity, myelin microscopy imaging

Running title: Investigating the long and short T_{1D} components correlation with myelin content. Comparison with R_1 and the macromolecular proton fraction (MPF).

Body text word count: 5833 words

INTRODUCTION

Myelination and demyelination mechanisms in the central nervous system (CNS) are a hallmark of aging and pathology. High specificity and sensitivity imaging tools are essential for an early detection of the variations in myelin content. The versatility of MRI has endowed the neuroscience community with numerous non-invasive MR markers sensitive to a variety of biophysical mechanisms and tissue microstructural features. In particular, the myelin sheath, composed of 40% of water and 60% of dry mass containing a high proportion of lipids (1), can be characterized by quantitative MRI measures probing both the water and the macromolecular components (2–6). While the issue of sensitivity has been addressed in multiple studies, the specificity to myelination of various quantitative and semi-quantitative MR metrics remains an open question.

The macromolecular proton fraction (MPF) (7) is a quantitative metric derived from the binary spin-bath model for MT (8,9), exhibiting a higher sensitivity to pathologically induced variations than the classical MT ratio according to preclinical (10–12) and clinical Multiple Sclerosis (MS) (13) studies. Standard methodology for MPF

measurement involves the acquisition of multiple MT-weighted images sampling a large number of offset frequencies and powers with regards to the preparation pulse in spoiled gradient echo (SPGR) sequences. However, the latest techniques for quantitative MT (qMT) allow the estimation of 3D MPF maps in a relatively short acquisition time (single-point qMT) (13–17).

The longitudinal relaxation rate (R_1) provides the basis for the most common contrast used in clinical routine. Besides the high dependence of in vivo R_1 quantification on the employed measurement technique (18), additional controversies are linked to the dominant factor influencing the R_1 contrast. While some publications show a clear relationship between iron deposition and R_1 (19,20), other studies suggest a greater and more significant contribution from macromolecules (21,22). Nonetheless, R_1 is shown to be a good predictor of the macromolecular tissue volume of the in vivo brain throughout the whole lifespan (23) and allows differentiation between cortical layers (24). In addition to macromolecules (25) and paramagnetic ions (26), R_1 is also sensitive to tissue hydration (27) and protein content (28).

Inhomogeneous magnetization transfer (ihMT) (29) is an MRI technique, weighted by $T_{1D,}$ the dipolar order relaxation time (30), an endogenous source of contrast driven by slow molecular dynamics and tissue microstructure (31,32). The sensitivity of ihMT to myelinated tissues (33–37) and myeloarchitectonic mapping (38) was validated in studies on healthy subjects, and for the characterization of myelin pathology in MS patients (39,40). A previous study comparing ihMT with histology (41) on genetically modified plp-GFP (proteolipid protein - Green Fluorescence Protein) mice highlighted

the impact of distinct T_{1D}-filtering strategies on the sensitivity and the specificity of ihMT to healthy myelinated tissues. As shown in Part I, high RF power and low duty-cycle ihMT preparations are sensitive to at least two T_{1D} components. While high-pass T_{1D}-filters can be used to adjust the signal contribution of long T_{1D} components (> 1 ms) to the total ihMT signal, sensitivity to the short component is achieved by linear combinations of data with different switching times, e.g., to produce an ihMT bandpass T_{1D}-filter in the 100 µs to 1 ms range. These filtering strategies inform on studies of microstructural correlates in healthy myelinated tissues using the corresponding ihMT images.

The aim of this work was thus to evaluate the specificity of ihMT high-pass and bandpass T_{1D}-filters to myelination and compare it to that of MPF and R_1. In addition to ihMTR, ihMTsat metrics compensated for R_1 relaxation effects and B_1^+ inhomogeneity effects arising from the excitation pulses were computed. The specificity to myelination was evaluated based on the estimated intercept and slope values (41) from linear regressions between the MR metrics and myelin quantifications using two microscopy measurements: plp-GFP fluorescence intensity signal and the LFB (Luxol Fast Blue) optical density.

METHODS

Animal experiments

Animal studies were conducted in agreement with the French guidelines for animal care from the French Department of Agriculture (Animal Rights Division), the directive

2010/63/EU of the European Parliament and of the Council of 22 September 2010 and approved by our institutional committee on Ethics in animal research (Comité d'Ethique de Marseille n°14, project authorization APAFIS#1747-2015062215062372v6).

Sixteen C57Bl/6J control mice were scanned in vivo at 10 weeks of age. Among them, 6 genetically modified mice expressing the green fluorescent protein (GFP) under the control of the *Plp* promoter which drives the expression of a major myelin component in the CNS – the proteolipid protein (PLP) (42) were sacrificed after the MR scans and analyzed by microscopy.

During scans under isoflurane anesthesia (1.5%, constant flow, 300 mL/min; Univentor 400 anesthesia unit, Zejtun, Malta), animal respiratory rate and temperature were monitored (SA Instruments, Stony Brook, NY, USA). Respiration was maintained at 100 ± 10 breaths-per-minute using minor adjustments to the isoflurane concentration. Temperature was maintained at 37.5 ± 0.5 °C using a heating blanket connected to a water bath system.

Quantitative MR protocol and image processing

MR experiments were performed on a preclinical 7T scanner (Bruker PharmaScan, Ettlingen, Germany), using a 72-mm body volume coil and a four-channel phased array receive-only MRI CryoProbe (Bruker, Ettlingen, Germany) for RF transmission and RF reception, respectively.

After positioning in the magnet isocenter, a field map-based shimming (acquisition time 1 min 22 s) was performed to optimize B_0 field homogeneity over the entire mouse brain.

Structural T_2-weighted (T_2w) images were acquired using a 2D multi-slice RARE sequence (RARE factor = 8, TE/TR = 32/5030 ms, matrix size 256x256, in-plane voxel size 78x78 μm^2, slice thickness 300 µm, 49 slices covering the whole brain, acquisition time TA = 5 mins 22 s). B_1^+ mapping was performed with the Actual Flip Angle imaging (AFI) method (43,44) ($TE/TR_1/TR_2$ = 2/15/60 ms, matrix size 48x48x44, 400x400x750 μm^3, FA = 60°, TA = 1 min 59 s) on the whole mouse brain.

R_1 maps

Variable Flip Angle VFA-SPGR sequences (TE/TR = 2.2/30.0 ms, TA = 9 mins 30 s) for R_1 quantification were acquired using FAs of 6°, 10°, and 25°. Data were fit to the Ernst equation (45) to estimate voxel-wise the R_1 values corrected for B_1^+ deviations.

Single-point MPF maps

An MT-prepared SPGR sequence (TE/TR = 2.2/30.0 ms, TA = 3 mins 10 s) was performed using a 10.25 ms off-resonance gaussian pulse for saturation with an offset frequency of 6 kHz and a flip angle of 600° (corresponding B_{1peak} = 9.1 µT and B_{1rms} = 5.0 µT) (17). According to the single-point strategy, the two-pool model for MT with optimal constrained parameters (17) was used to estimate MPF maps with B_1^+ correction. The VFA-SPGR acquisition at FA = 10° was used as a reference image.

IhMTR maps

T_{1D}-weighted ihMT images were acquired with the sequence presented in Part 1 and the protocol described in Part I. In brief, slab-selective 3D low duty-cycle (35,46) ihMTRAGE (47) sequences were acquired with different dual-frequency offset switching times (Δt) (Saturation: 15 bursts of N_p = 8 Hann-shaped pulses, pulse duration pw = 0.5 ms, B_{1peak} =42.4 μT, offset frequency Δf = 10 kHz, burst repetition time BTR = 60 ms, total saturation time τ = 900 ms, corresponding root-mean-squared saturation power calculated over the total saturation time B_{1RMS}^{SAT} = 6.7 μT and RF duty-cycle DC = 6.7%. Readout: TE/TR = 2.1/2200.0 ms, matrix size 192x192x8, voxel size 100x100x750 μm^3, cartesian centric-out in the RAGE partition). IhMT images were calculated from the difference between the single and the dual-frequency offset MT images. The latter were obtained either with cosine-modulated pulses (dual-frequency switching time virtually corresponding to Δt = 0.0 ms and referenced hereafter as $\Delta t_{0.0}$), either with frequency-alternating pulses and Δt = 0.8 ms, and Δt = 3.2 ms (referenced hereafter as $\Delta t_{0.8}$ and $\Delta t_{3.2}$, respectively). Based upon the results of Part I, the selected Δt values led to ihMT high-pass T_{1D}-filters with increasing T_{1D} cutoff values. In addition, an ihMT bandpass T_{1D}-filter, isolating components within the 100 μs to 1 ms range, was obtained by subtracting ihMT images derived from the $\Delta t_{0.0}$ and $\Delta t_{0.8}$ configurations ($\Delta t_{0.0}$ - $\Delta t_{0.8}$). For each configuration, a reference image with zero power saturation, MT_0, was also acquired. IhMTR maps were calculated:

$$ihMTR = \frac{(MT^{+} + MT^{-}) - (MT^{\pm} + MT^{\mp})}{MT_0} \quad \text{equation 1}$$

For SNR consideration, a total number of 6, 12, and 18 repetitions of MT^{+} and $MT^{\pm}$ images were acquired for the $\Delta t_{0.0}$, $\Delta t_{0.8}$, and $\Delta t_{3.2}$ respectively, leading to acquisition times of 8 mins 40 s, 11 mins 20 s, and 22 mins.

IhMTsat maps

IhMT metrics corrected for R_1 relaxation and B_1^+ inhomogeneity effects on the readout excitation pulses (ihMTsat) were derived based on a strategy initially proposed for MT imaging (48), and more recently customized to the ihMTRAGE framework (38).

Equations (A10) from Munsch et al. (38) were used to derive the longitudinal magnetization at the first RAGE segment, taking into account all the events in the sequence (i.e., saturation and free precession periods, and readout pulses). The attenuation factor (δ), described under the hypothesis of a single instantaneous saturation (6.4 ms burst), was estimated using the Brent's root finding method for both single- and dual- offset saturations to derive ihMTsat.

Python-based wrappers are made available: 1) for R_1 and MPF maps calculation at: https://github.com/lsoustelle/SP_qMT_proc (hash cc210c2); 2) for ihMTsat maps calculation at: https://github.com/lsoustelle/ihmt_proc (hash 34bd8b3).

A diagram summarizing the acquired raw images and the processing steps required to build the R_1, MPF, ihMTR and ihMTsat metrics is provided in Figure 1.

MR images quantification

3D-templates of ihMTR, ihMTsat, MPF and R_1 were constructed and registered in the same reference as the T_2w templates. A comprehensive description of the template construction from the individual images of the 16 mice, and the segmentation of Regions-of-Interest (ROIs) is provided in the appendix of Part I.

ROI-wise analyses (MRI vs. microscopy)

ROI-wise analyses on each of the 6 plp-GFP mice at 3 bregma levels (+ 0.7 mm, - 1.0 mm and - 3.2 mm from bregma), corresponding to the microscopy slices, were performed for comparison between MR and microscopy metrics. ROI-based quantification was performed from the averaged values in seven structures (mCC – medial corpus callosum, INT – internal capsules, OPT – optical tract, TH – thalamus, CP – caudoputamen, CTX- cerebral cortex, and HIP – hippocampal region) for all MR and microscopy metrics.

Voxel-wise analyses (MPF vs. ihMT T_{1D}-filters)

A brain mask was generated from a hard thresholding procedure based on the MPF template image, and applied to all co-registered templates (ihMTR, ihMTsat, MPF and T_2w). In order to eliminate the CSF contribution in view of whole-brain voxel-wise analyses, a 3-classes k-means clustering was performed using Atropos (49) from ANTs based on the skull-stripped T_2w template image. Voxels were then retrieved for each common slice of the ihMTR, ihMTsat and MPF templates. Analyses between MPF and ihMT metrics were done on the voxel-wise averaged metrics of the 16 mice.

Microscopy images quantification

After in vivo MR experiments, the 6 plp-GFP mice were sacrificed (ketamine 150 mg/kg with xylazine 15 mg/kg) and intracardially perfused with a fixative of (4% paraformaldehyde). Mouse brains were then extracted, post-fixed for 2 h in 4% paraformaldehyde and cryopreserved overnight in 20% sucrose. Frozen brains were sectioned into 20 µm thick histological slices (Cryostat Leica CM305S) in the rostro-caudal direction at 3 different levels (+ 0.7 mm, - 1.0 mm and - 3.2 mm from bregma) for plp-GFP fluorescence and LFB optical density analyses. ROIs were manually placed on the microscopy images by two different observers (J.B. and M.C.) in the seven brain structures chosen for the ROI-wise MRI quantification, using a mouse brain atlas as reference.

Plp-GFP fluorescence

Six mouse brains were used for the plp-GFP fluorescence analysis. For each level, three slices were acquired using a Zeiss fluorescence microscope with a 5x objective and a fixed exposure time. Background noise was measured in the ventricles and subtracted. Analyses were performed using the ImageJ software (National Institutes of Health, Bethesda, MD) and the mean value in each of the seven structures was computed. The resulting signal was normalized, taking as a reference the signal in the internal capsules.

LFB optical density

Three mouse brains were used for the LFB staining analysis. Brain sections were post-fixed in methanol for 2 mins at -20°C, then rinsed in ethanol/acetic acid (96/4) for 5

mins. Sections were then stained in LFB (Sigma-Aldrich) 0.1% diluted in ethanol/acetic acid during 3 h at 60°C. After a short rinse in ethanol 96%, sections were decolorized in lithium carbonate 0.05% for 1 min and rinsed in ethanol 70%. Finally, sections were dehydrated through increasing ethanol gradients (from 70% to 100%) and mounted in Eukitt (VWR). Pictures were taken with a Zeiss AxioImager microscope with a 5x objective and optical density was measured using ImageJ, as described by Khodanovich et al. (12). Briefly, the mean intensity of the red channel was measured in RGB images as a quantity characterizing the complementary blue channel saturation. Background signal was also measured in the ventricle, and LFB optical density was calculated as follows: (1 – red mean intensity / background intensity). Signals were normalized to the signal of the internal capsules.

Analyses and Statistics

MRI vs. microscopy

Mean and standard deviation values in the seven averaged ROIs from the three bregma levels of the 6 plp-GFP mice were used to evaluate the specificity of each MR metric and the sensitivity of ihMTR and ihMTsat configurations. The normality of data and that of residuals in regression analyses was assessed in JMP (v.16.0.0; SAS Institute, Cary, NC) using the Shapiro-Wilk test. Pearson's correlations and linear regressions were performed for a total of ten response variables (ihMT high-pass and bandpass T_{1D}-filters, MPF and R_1) and two predictor variables (normalized plp-GFP and LFB signal intensities).

Comparisons between the linear regression analyses

A one-way analysis of covariance (ANCOVA) with interaction in JMP was used to test for significance in differences between pairs of slopes and intercepts. Steiger's modification of Dunn and Clark's z approach (50) and the Zou's confidence interval (51) from the *cocor* package (52) for overlapping correlations based on dependent groups in R (v.1.4.1106; RStudio, PBC, Boston, MA, US) was used to test for significance in differences between pairs of correlation coefficients.

Two types of comparison analyses were performed. First, by considering the MR metrics as the common variable, we investigated whether the MR metrics behave significantly different when associated with plp-GFP or LFB signals. Second, by considering one of the microscopy metrics as the common variable, we investigated whether there is an MR metric that associates significantly better with each of the two microscopy references.

Specificity assessment

The specificity to myelin of all MR metrics (41) when referenced to either plp-GFP or LFB measurements was assessed as the fraction of MRI signal associated with myelin over the total signal, calculated as:

$$Specificity = \frac{slope * X_{max}}{slope * X_{max} + Y\_intercept} \qquad \text{equation 2}$$

Where *slope* and *Y_intercept* are defined as the coefficients of the affine functions derived from the linear regression analyses. The *Y_intercept* is by definition the MRI signal measured in the absence of microscopy signal (i.e., for X = 0), and hence in the

absence of myelin. The product $slope*X_{max}$ represents the maximum MRI signal corresponding to X_{max}, the maximum of microscopy signal (and hence the maximum of myelin content). The product $slope*X_{max}$ thus corresponds to the fraction of ihMT signal associated to myelin. The specificity, as defined here, is thus relative to a reference anatomical structure, in this case, the internal capsules. Note that for the specificity calculation, the *Y_intercept* values were corrected for the offset corresponding to the values of MR metrics in pure water: 0.3 Hz for R_1 (53) and 0.0% for the MT-based metrics.

Sensitivity assessment

Sensitivities were evaluated for ihMTR and ihMTsat metrics, respectively based on the slope values resulting from linear regression analyses with plp-GFP and LFB.

MPF vs. ihMT T_{1D}-filters

Pearson's correlations and linear regression analyses were performed between MPF and ihMT T_{1D}-filters (ihMTR and ihMTsat) voxel-wise quantifications for a total of 51 common slices in the template space. Pairs of correlation coefficients and intercepts for the ihMTR and ihMTsat configurations were tested for significant differences using a Kruskal-Wallis test with post-hoc pairwise comparisons.

RESULTS

MR templates for R_1, MPF, ihMTR and ihMTsat at +0.7 mm, -1.0 mm, and -3.2 mm from bregma are presented in Figure 2 along with the corresponding plp-GFP intensity images. Qualitatively, R_1 showed a lower contrast between White Matter (WM) and

Grey Matter (GM) tissues compared to ihMTR, ihMTsat and MPF. In addition, WM/GM contrast was qualitatively improved in the ihMTsat images as compared to ihMTR. Quantification of all metrics in each of the segmented structures are reported in Supporting Information Table S1.

Plp-GFP vs. LFB

Linear regression and Pearson's correlation analyses between LFB and plp-GFP normalized signals (Figure 3) revealed a strong and significant correlation ($r^2 = 0.83$, $p < 0.001$) with a positive significant slope (1.12 ± 0.12, $p < 0.001$) and a non-significant intercept (-0.16 ± 0.09, $p = 0.11$).

MRI vs. microscopy analyses

Outcomes of the linear regressions between the MR metrics and the plp-GFP and LFB signals are shown in Table 1, along with the corresponding scatter plots in Figure 4. Residuals followed a normal distribution according to the Shapiro Wilk test ($p > 0.05$). Strong and significant correlation coefficients were obtained for ihMT high-pass T_{1D}-filters (ihMTR ($\Delta t_{0.0}$, $\Delta t_{0.8}$, $\Delta t_{3.2}$) and ihMTsat ($\Delta t_{0.0}$, $\Delta t_{0.8}$, $\Delta t_{3.2}$)) and MPF with regards to plp-GFP ($r^2 \geq 0.79$, $p < 0.001$) and LFB ($r^2 \geq 0.87$, $p < 0.001$). Lower but significant correlation coefficients corresponded to R_1 and the ihMT bandpass T_{1D}-filter. Estimated Y_intercept values were generally significantly different than zero ($p < 0.05$), except for the intercept of ihMTR ($\Delta t_{3.2}$) and ihMTsat ($\Delta t_{0.8}$, $\Delta t_{3.2}$) when compared to plp-GFP. Globally, the specificity to myelination for the investigated MR metrics was higher for associations with plp-GFP than for associations with LFB except for the ihMT

bandpass T_{1D}-filter, for which similar specificity was found when plp-GFP or LFB was used for association. The specificity of the ihMT high-pass T_{1D}-filters exhibited an increasing trend with increasing Δt, while ihMTsat specificity values were superior to those of ihMTR for all Δt values.

Comparisons between the linear regression analyses: MR metrics as the common variable

No significant differences were found between pairs of correlation coefficients and pairs of slopes when MR metrics were considered as the common variable, suggesting similar sensitivities of each MR metric to the two microscopy references. However, significant differences ($p < 0.05$) were found between pairs of intercept values for all the MR metrics, except for the ihMT bandpass T_{1D}-filter and R_1 (Supporting Information Table S2).

Comparisons between the linear regression analyses: microscopy metrics as the common variable

The significance of differences between pairs of overlapping correlation coefficients with either plp-GFP or LFB as the common variable are presented in Table 2. Significant differences were generally found when comparing ihMT bandpass T_{1D}-filter or R_1 correlation coefficients with ihMT high-pass T_{1D}-filters or MPF correlation coefficients. For ihMT metrics, the significance of differences between pairs of intercepts and pairs of slopes with either plp-GFP or LFB as the common variable are presented in Table 3. Significant differences were noticed for comparisons between all

pairs of intercepts, except for comparisons between $\Delta t_{0.0}$ with $\Delta t_{0.0} - \Delta t_{0.8}$ (ihMTR and ihMTsat) and $\Delta t_{0.8}$ with $\Delta t_{3.2}$ (ihMTR and ihMTsat) for associations with plp-GFP, and between $\Delta t_{0.8}$ and $\Delta t_{0.0} - \Delta t_{0.8}$ (ihMTR and ihMTsat) for associations with LFB. Differences between pairs of slopes were significantly different for all ihMTR and ihMTsat metrics ($p < 0.05$), except for comparisons between ihMTR ($\Delta t_{0.0} - \Delta t_{0.8}$) and ihMTR ($\Delta t_{3.2}$) for associations with LFB or ihMTsat ($\Delta t_{0.0} - \Delta t_{0.8}$) with ihMTsat ($\Delta t_{3.2}$) for associations with plp-GFP and LFB.

MPF vs. ihMT T_{1D}-filters analyses

Figure 5 and Figure 6 represent the distribution of ihMT high-pass and bandpass T_{1D}-filters as compared to the distribution of MPF data points by means of 2D histograms and illustrate the corresponding slices. The signal intensity distribution is different between the various slices as a consequence of a varying number of voxels corresponding to WM (high signal intensity) or GM (low signal intensity) tissues. Here we can notice the importance of the ihMTsat metric in re-establishing the signal distribution in each slice. The effect is more pronounced for the bandpass T_{1D}-filter.

Correlations of MPF with ihMT high-pass T_{1D}-filters (Figure 7a) were significant and strong ($r^2 > 0.64$, $p < 0.001$ for ihMTR, and $r^2 > 0.72$, $p < 0.001$ for ihMTsat) for all slices. Significant ($p < 0.001$) but lower and more dispersed correlations were obtained for the ihMT bandpass T_{1D}-filter. All estimated slope and intercept values were significantly different from zero ($p < 0.001$). Intercepts increased for increasing Δt, for ihMT high-pass T_{1D}-filters. Lowest intercept values were obtained for ihMT high-pass

T_{1D}-filters with the lowest cutoff ($\Delta t_{0.0}$) and for the ihMT bandpass T_{1D}-filter (Figure 7b). Examples of linear regression analyses are given in Supporting Information, figures S1 and S2.

DISCUSSION

Increasing the fraction of ihMT signal corresponding to long T_{1D}s enhances the specificity to myelination.

The assessment of the specificity was based on the evaluation of the intercept and slope values resulting from linear regression analyses between the MR metrics and the normalized signals of two microscopy references. In this approach, the intercept and slope values are competitive estimates. For the specificity to increase with the lengthening of Δt, the decrease in the intercept must be more important than the decrease in the slope. According to the results in Part 1, this is due to the disproportionate attenuation of long and short T_{1D} signals as Δt increases. High-pass T_{1D}-filters increase the fraction of ihMT signal corresponding to long T_{1D}s and reduce that of short T_{1D}s (Part I, Table 2), leading to an enhanced specificity to myelination.

The specificity dependence on Δt observed in this study for ihMT high-pass T_{1D}-filters is in agreement with previously reported results (41). However, specificity values corresponding to the plp-GFP reference obtained here are generally higher compared to those reported by Duhamel et al. (41). While a discrepancy arising from a calibration bias of the plp-GFP signal may not be excluded, several differences regarding the RF saturation parameters with a direct influence on the T_{1D} filtering mechanisms might

explain the improvement in our results. The main advantage of this work consisted of the use of a modified version of ihMT (54) allowing us to maintain constant pulse power throughout all ihMT acquisitions. Thus, the sole effects of the switching time were consistently isolated, and the specificity was more accurately assessed and compared across ihMT variants. Furthermore, partial volume effects were approximately 13 times lower per voxel in the current work, and the mouse cohort investigated here was larger.

Short T_{1D} components are poorly correlated with myelin.

Since the intercept designates the value of a specific MR metric obtained for a null plp-GFP or LFB signal, it actually relates to the part of the MR signal corresponding to a non-myelin source. Interestingly, for associations with the plp-GFP signal, the $\Delta t_{0.0}$ configuration containing a high amount of signal originating from the short T_{1D}s (Part I, Table 2) had a slightly higher, but not significantly different intercept as compared to the band-pass T_{1D}-filter which mainly isolates the short T_{1D}s. As Δt increased, the fraction of signal corresponding to the short T_{1D}s diminished as compared to the fraction of signal corresponding to long T_{1D}s, and the intercept decreased as well. For example, the intercept of the $\Delta t_{3.2}$ configuration which had a higher signal contribution from the long T_{1D}s, was significantly different from the intercept of both of the $\Delta t_{0.0}$ and $\Delta t_{0.0} - \Delta t_{0.8}$ configurations for associations with both plp-GFP and LFB signals. In addition, the r^2 correlation coefficient of the band-pass T_{1D}-filter was significantly lower than that of any of the high-pass T_{1D}-filters containing long T_{1D}s in various amounts. This allowed us to conclude that the non-myelin part of the ihMT signal is preferentially associated to the signal of short T_{1D} components.

However, the source of the various T_{1D}s in in vivo tissues has still to be determined. While some short T_{1D}s could also be present in myelin tissue, another important possible source could be the non-myelin macromolecules with a restrained movement, presumably associated with glial cells. For example, the fibrous astrocytes with elongated morphology and processes aligned with the myelinated fibers present in WM (55), are a potential candidate for the short T_{1D} component. Further dedicated studies will however be required to confirm the precise nature of short T_{1D} non-myelin molecules revealed by the ihMT bandpass T_{1D}-filter.

IhMTsat improves the specificity of ihMT to myelination.

The correction for confounding B_1^+ inhomogeneity and R_1 relaxation effects in the ihMT signal is vital for proper clinical studies, reproducibility, and multi-site comparisons. Moreover, as shown in this study, the relative WM/GM contrast is qualitatively enhanced for ihMTsat and the specificity to myelination is considerably improved. While various available approaches (48,56,57) demonstrated their utility, the ihMTsat approach presented by Munsch et al. (38) and implemented here has the advantage of a minimum number of assumptions.

MR metrics specificity is higher for associations with plp-GFP, than with LFB.

The two microscopy references investigated in this study led to non-identical specificity values for MR metrics and generally higher values for associations with plp-GFP (7% higher for MPF and higher than 11% for ihMT high-pass T_{1D}-filters). For R_1 and the ihMT bandpass T_{1D}-filter the difference in the absolute specificity values calculated

with either plp-GFP or LFB was inferior to 5%. Additionally, for these metrics, linear regression analyses presented non-significant differences in the intercept and slope values for associations with plp-GFP and LFB, potentially suggesting a non-significant difference between specificities.

The distinct underlying sources of signal for the two microscopy references may explain the discrepancies between specificity values for MPF and ihMT high-pass T_{1D}-filters. Lipids and proteins alike contribute to the MRI contrast (58,59), but disparate MT effects have been observed depending on the molecules. Increased MT effects were obtained for cerebrosides as a result of a higher number of exchangeable protons and greater accessibility to free water (60). Conversely, phospholipids with fewer exchangeable protons such as dimyristoylphosphatidylcholine (DMPC) and phosphatidylcholine (PC) were found to have reduced MT effects (60,61). Although such studies only considered a limited number of myelin components, the lower specificity obtained for associations between the MT-derived metrics (ihMTR, ihMTsat, and MPF) and LFB might be explained by a lower sensitivity of MT effects to the presence of certain phospholipids, as opposed to the LFB quantifications (62,63). For example, PC is a major lipid of biological membranes accounting for 12% of the myelin lipids in rodents (64). In addition, phospholipids present in the membrane of other neural cells, such as astrocytes (65), are also stained by LFB, thereby reducing the specificity of LFB for the myelin membrane.

On the other hand, transgenic mice expressing the green fluorescent protein driven by the proteolipid protein gene promoter have been developed to investigate cells in the

oligodendrocyte lineage (66,67), offering a high specificity to mature oligodendrocytes in the adult brain (68) and thus a more specific biomarker for the myelin membrane.

MPF is weighted toward short T_{1D} components.

MPF quantifications in the various ROIs are consistent with previously reported results using the single-point method (17). The extrapolated specificity of MPF calculated with the slope and intercept values reported by Khodanovich et al. (12) for associations with LFB on C57BL/6 healthy mice is higher by 15% as compared to the specificity in our study (66% vs. 51%). Both intercept and slope values are lower in our study. A lower number of data points for the linear regression analyses in this study combined with microscope calibration biases and a different staining and storage procedure of the brain slices might explain this difference.

Generally, the lower specificity of MPF to myelination can be explained by the underlying sensitivity of the saturation efficacy in z-spectrum analyses. Although dipolar order effects were shown to have moderate to significant impact on the accuracy of MT data fitting depending on the investigated tissue (9,69), the binary spin-bath model used for MPF estimation does not consider any dipolar order contribution. This has particularly problematic consequences. Long RF pulses with low instantaneous power as used in MT-prepared SPGR sequences are inefficient in creating dipolar order effects with regards to the short T_{1D} components. The saturation of the corresponding Zeeman pools is therefore not altered, and the MT effects of the short T_{1D} components are well modeled by the two-pool model. Conversely, for longer

T_{1D} components, the RF pulses generate dipolar order effects, which alter the corresponding Zeeman pool saturation, but are not considered by the two-pool model. The MT effects of long T_{1D} components are thus not appropriately modeled. The estimated MPF derived from the classical binary spin-bath model is therefore preferably weighted toward short T_{1D} components, associated with a low specificity to myelination.

These observations are further confirmed by the voxel-wise regression analyses between MPF and ihMT. The lowest intercept values and thus the ihMT configurations the closest to being in a direct proportionality relationship with MPF correspond to ihMT ($\Delta t_{0.0}$), the signal of which is weighted by short T_{1D} components and ihMT ($\Delta t_{0.0}$ - $\Delta t_{0.8}$), which specifically isolates short T_{1D}s.

Thereupon, the effects of dipolar interactions on the MPF estimations in in vivo brain tissues and for the experimental scenarios used here should be considered in the future. Alternatively, cosine-modulated RF saturation pulses, which decouple Zeeman and dipolar order pools, should be employed for MPF estimations when using the classical binary-spin bath model.

R_1, MPF and ihMT: practical considerations for myelin imaging.

From a clinical point of view, the ideal technique for myelin imaging should be highly sensitive and specific, have a straightforward computation and relatively short acquisition time. None of the techniques investigated in this work meets all the criteria.

In terms of sensitivity, R_1, MPF, and to a lesser extent the $\Delta t_{0.0}$ ihMT configuration offer the best SNR performance and are also moderately to strongly correlated to myelination (r^2 = 0.67 for R_1 and > 0.8 for MPF and ihMT). Unfortunately, these are also the least specific metrics due to a non-negligible contribution from non-myelin tissue to their signal, reflected by the high *Y_intercept* values. Almost all the investigated MR metrics have non-zero *Y_intercept*, which is not surprising since macromolecules other than myelin contribute to T_1 relaxation, the MPF size, and the dipolar order exists in other macromolecules as well. An accurate estimation of each metric in non-myelin neuronal tissue would allow compensating for the non-zero *Y_intercept*, but this is not an easy task and could be further complicated in the case of pathology.

In this context, a great advantage of ihMT over the other metrics is that there is no need to accurately quantify and correct for the signal of non-myelin neuronal tissue to improve the specificity. A better myelin selectivity can be achieved through the lengthening of Δt, and hence for specificity purpose, ihMT high-pass T_{1D}-filters ($\Delta t \geq 0.8$ ms) are very good candidates although they have lower SNR. The group standard deviation of ihMTR values in the seven investigated ROIs (Table S1) represents in average less than 7% of the mean ihMTR value for $\Delta t_{0.0}$ but more than 17% for $\Delta t_{3.2}$. Lengthening Δt over 3.2 ms would probably induce a prohibitive SNR for accurate specificity measurements. Here, the minimum SNR obtained for $\Delta t_{3.2}$ (isolating mainly long T_{1D}s) and the bandpass T_{1D}-filter (isolating mainly short T_{1D}s) was high enough to

accurately demonstrate a higher specificity of $\Delta t_{3.2}$ than that of the bandpass T_{1D}-filter by more than 1.5 standard errors.

Regarding the computational simplicity (Figure 1), ihMTR is the only metric derived from a simple combination of the raw images. Other metrics require a more advanced knowledge of their respective model, hence complicating their derivation. In terms of acquisition time, ihMTR ($\Delta t < 3.2$ ms) and R_1 required less than 12 minutes, while ihMTR ($\Delta t_{3.2}$) and MPF required more than 15 minutes. These acquisition times might appear too long from a clinical perspective, but they are in line with typical preclinical acquisition times for parametric imaging with a 100 µm in-plane resolution. Moreover, in clinical applications, the nominal resolution is lower (~1.5 – 2 mm), and the degree of myelination is higher (leading to higher ihMTR values), thus the ihMT high-pass T_{1D} filters strategies are routinely feasible ($\Delta t = 0.0$ ms (47) and $\Delta t > 0.0$ ms (35)).

To summarize, the higher sensitivity of R_1, MPF and the $\Delta t_{0.0}$ high-pass T_{1D}-filter (ihMTR/ihMTsat) can be advantageously used for the general characterization of diseases for which myelin alterations are part of the pathological processes. On the other hand, high-pass T_{1D}-filters with long Δt values should be preferred to investigate whether myelin is specifically altered in pathologies.

Limitations

First, an important limitation in the assessment of the specificity in the current study was the lower spatial resolution of the MR slices (750 µm) as compared to that of the microscopy slices (20 µm). To partially overcome this issue, three slices of 20 µm were

sampled inside the corresponding MR slice thickness of 750 μm and the resulting signals were averaged. Second, the specificity as defined here is not an absolute measure, but rather a relative estimation referenced to the signal of a known highly myelinated structure (internal capsules). Normalization to another structure with a higher degree of myelination may yield slightly different specificity values. Finally, for a more comprehensive qualitative and quantitative analysis on the specificity of different MR metrics, future studies should comprise a larger number of microscopy markers including antibodies for other myelin specific proteins, lipid dyes or even more advanced techniques such as Coherent Anti-Stokes Raman Spectroscopy (CARS) (70) which can be tuned to the specific vibrational frequency of methylene groups present along the lipid chains. Comparison with other MR metrics putatively sensitive to myelin but whose contrast rely on different mechanisms, e.g., Myelin Water Fraction, should also be performed (71).

CONCLUSIONS

The specificity to myelination of ihMT high-pass and bandpass T_{1D}-filters, MPF and R_1 was assessed using two histological reference techniques for myelin imaging. Lengthening of the Δt leads to an increase in the fraction of signal corresponding to long T_{1D}s and thus provided higher specificities to myelination for ihMT high-pass T_{1D}-filters, albeit at the cost of lower sensitivity. The correction for T_1/B_1 effects allowed us to further enhance the specificity of ihMT to myelination and generate images with higher WM/GM contrast.

The ihMT bandpass T_{1D}-filter, which isolates the short T_{1D} components (< 1 ms) whose nature will require future dedicated studies, provided lower specificity values. Additionally, an important contribution of short T_{1D} components to the MPF estimation can explain the lower specificity of MPF to myelination as compared to the ihMT high-pass T_{1D}-filters.

Future studies with ihMT T_{1D}-filters would be of particular interest when analyzing ihMT signal variations in pathological brain conditions. As T_{1D} is sensitive to membrane organization (31), the myelin structural transformation occurring in some diseases (e.g., loss of the normal compact multilamellar structure observed in MS (72)) might induce changes on the short and long T_{1D} components, and hence modify the ihMT signal in the brain. Thus, ihMT bandpass and high-pass T_{1D}-filters with properly adjusted T_{1D} cutoff values could determine the ranges of T_{1D} components affected by the pathological processes.

Acknowledgements

This work was funded by ANR-17-CE18-0030, VERISMO project and partly funded by France Life Imaging (grant ANR-11-INBS-0006), ARSEP 2021 and CARNOT STAR 2020. Authors thank Nathalie Cuge for animal handling.

References

1. Morell P, Quarles RH. Characteristic Composition of Myelin. Basic Neurochem. Mol. Cell. Med. Asp. 6th Ed. 1999.

2. Mancini M, Karakuzu A, Nichols T, Cohen-Adad J, Cercignani M, Stikov N. The quest for measuring myelin with MRI – An interactive meta-analysis of quantitative comparisons with histology. Neuroscience; 2020. doi: 10.1101/2020.07.13.200972.

3. Piredda GF, Hilbert T, Thiran J, Kober T. Probing myelin content of the human brain with MRI: A review. Magn. Reson. Med. 2020 doi: 10.1002/mrm.28509.

4. van der Weijden CWJ, García DV, Borra RJH, et al. Myelin quantification with MRI: A systematic review of accuracy and reproducibility. NeuroImage 2021;226:117561 doi: 10.1016/j.neuroimage.2020.117561.

5. Lazari A, Lipp I. Can MRI measure myelin? Systematic review, qualitative assessment, and meta-analysis of studies validating microstructural imaging with myelin histology. Neuroscience; 2020. doi: 10.1101/2020.09.08.286518.

6. Weiger M, Froidevaux R, Baadsvik EL, Brunner DO, Rösler MB, Pruessmann KP. Advances in MRI of the myelin bilayer. NeuroImage 2020;217:116888 doi: 10.1016/j.neuroimage.2020.116888.

7. Yarnykh VL. Pulsed Z-spectroscopic imaging of cross-relaxation parameters in tissues for human MRI: Theory and clinical applications. Magn. Reson. Med. 2002;47:929–939 doi: https://doi.org/10.1002/mrm.10120.

8. Yeung HN, Adler RS, Swanson SD. Transient Decay of Longitudinal Magnetization in Heterogeneous Spin Systems under Selective Saturation. IV. Reformulation of the Spin-Bath-Model Equations by the Redfield-Provotorov Theory. J. Magn. Reson. A 1994;106:37–45 doi: 10.1006/jmra.1994.1004.

9. Morrison C, Stanisz G, Henkelman RM. Modeling magnetization transfer for biological-like systems using a semi-solid pool with a super-Lorentzian lineshape and dipolar reservoir. J. Magn. Reson. B 1995;108:103–113 doi: 10.1006/jmrb.1995.1111.

10. Rausch M, Tofts P, Lervik P, et al. Characterization of white matter damage in animal models of multiple sclerosis by magnetization transfer ratio and quantitative mapping of the apparent bound proton fraction f. Mult. Scler. Houndmills Basingstoke Engl. 2009;15:16–27 doi: 10.1177/1352458508096006.

11. Underhill HR, Rostomily RC, Mikheev AM, Yuan C, Yarnykh VL. Fast bound pool fraction imaging of the in vivo rat brain: Association with myelin content and validation in the C6 glioma model. NeuroImage 2011;54:2052–2065 doi: 10.1016/j.neuroimage.2010.10.065.

12. Khodanovich MY, Sorokina IV, Glazacheva VY, et al. Histological validation of fast macromolecular proton fraction mapping as a quantitative myelin imaging method in the cuprizone demyelination model. Sci. Rep. 2017;7 doi: 10.1038/srep46686.

13. Yarnykh VL, Bowen JD, Samsonov A, et al. Fast Whole-Brain Three-dimensional Macromolecular Proton Fraction Mapping in Multiple Sclerosis. Radiology 2015;274:210–220 doi: 10.1148/radiol.14140528.

14. Yarnykh VL. Fast macromolecular proton fraction mapping from a single off-resonance magnetization transfer measurement. Magn. Reson. Med. 2012;68:166–178 doi: 10.1002/mrm.23224.

15. Yarnykh VL, Kisel AA, Khodanovich MY. Scan–Rescan Repeatability and Impact of B_0 and B_1 Field Nonuniformity Corrections in Single-Point Whole-Brain Macromolecular Proton Fraction Mapping. J. Magn. Reson. Imaging 2020;51:1789–1798 doi: 10.1002/jmri.26998.

16. Soustelle L, Antal MC, Lamy J, Rousseau F, Armspach J-P, Sousa PL de. Correlations of quantitative MRI metrics with myelin basic protein (MBP) staining in a murine model of demyelination. NMR Biomed. 2019;32:e4116 doi: 10.1002/nbm.4116.

17. Soustelle L, Antal MC, Lamy J, Harsan L, Loureiro de Sousa P. Determination of optimal parameters for 3D single-point macromolecular proton fraction mapping at 7T in healthy and demyelinated mouse brain. Magn. Reson. Med. 2020 doi: 10.1002/mrm.28397.

18. Stikov N, Boudreau M, Levesque IR, Tardif CL, Barral JK, Pike GB. On the accuracy of T1 mapping: Searching for common ground. Magn. Reson. Med. 2015;73:514–522 doi: https://doi.org/10.1002/mrm.25135.

19. Ogg RJ, Steen RG. Age-related changes in Brain T1 are correlated with iron concentration. Magn. Reson. Med. 1998;40:749–753 doi: https://doi.org/10.1002/mrm.1910400516.

20. Vymazal J, Hajek M, Patronas N, et al. The quantitative Relation Between T1-Weighted and T2-Weighted MRI of Normal gray Matter and iron concentration. J. Magn. Reson. Imaging 1995;5:554–560 doi: https://doi.org/10.1002/jmri.1880050514.

21. Stüber C, Morawski M, Schäfer A, et al. Myelin and iron concentration in the human brain: A quantitative study of MRI contrast. NeuroImage 2014;93:95–106 doi: 10.1016/j.neuroimage.2014.02.026.

22. Rooney WD, Johnson G, Li X, et al. Magnetic field and tissue dependencies of human brain longitudinal 1H2O relaxation in vivo. Magn. Reson. Med. 2007;57:308–318 doi: 10.1002/mrm.21122.

23. Yeatman JD, Wandell BA, Mezer AA. Lifespan maturation and degeneration of human brain white matter. Nat. Commun. 2014;5:4932 doi: 10.1038/ncomms5932.

24. Lutti A, Dick F, Sereno MI, Weiskopf N. Using high-resolution quantitative mapping of R1 as an index of cortical myelination. NeuroImage 2014;93:176–188 doi: 10.1016/j.neuroimage.2013.06.005.

25. Manning AP, MacKay AL, Michal CA. Understanding aqueous and non-aqueous proton T1 relaxation in brain. J. Magn. Reson. 2021;323:106909 doi: 10.1016/j.jmr.2020.106909.

26. Lauffer RB. Paramagnetic metal complexes as water proton relaxation agents for NMR imaging: theory and design. https://pubs.acs.org/doi/pdf/10.1021/cr00081a003. Published May 6, 1987. Accessed June 27, 2021 doi: 10.1021/cr00081a003.

27. Filo S, Shtangel O, Salamon N, et al. Disentangling molecular alterations from water-content changes in the aging human brain using quantitative MRI. Nat. Commun. 2019;10:3403 doi: 10.1038/s41467-019-11319-1.

28. Zhong J, Gore JC, Armitage IM. Quantitative studies of hydrodynamic effects and cross-relaxation in protein solutions and tissues with proton and deuteron longitudinal relaxation times. Magn. Reson. Med. 1990;13:192–203 doi: 10.1002/mrm.1910130203.

29. Varma G, Duhamel G, de Bazelaire C, Alsop DC. Magnetization transfer from inhomogeneously broadened lines: A potential marker for myelin: Magnetization Transfer from Inhomogeneously Broadened Lines. Magn. Reson. Med. 2015;73:614–622 doi: 10.1002/mrm.25174.

30. Varma G, Girard OM, Prevost VH, Grant AK, Duhamel G, Alsop DC. Interpretation of magnetization transfer from inhomogeneously broadened lines (ihMT) in tissues as a dipolar order

effect within motion restricted molecules. J. Magn. Reson. 2015;260:67–76 doi: 10.1016/j.jmr.2015.08.024.

31. Dufourc EJ, Mayer C, Stohrer J, Althoff G, Kothe G. Dynamics of phosphate head groups in biomembranes. Comprehensive analysis using phosphorus-31 nuclear magnetic resonance lineshape and relaxation time measurements. Biophys. J. 1992;61:42–57 doi: 10.1016/S0006-3495(92)81814-3.

32. Annabestani R, Cory D. Dipolar Relaxation Mechanism of Long Lived States in Methyl Groups. ArXiv170403035 Quant-Ph 2017.

33. Girard OM, Prevost VH, Varma G, Cozzone PJ, Alsop DC, Duhamel G. Magnetization transfer from inhomogeneously broadened lines (ihMT): Experimental optimization of saturation parameters for human brain imaging at 1.5 Tesla: Optimizing Saturation Parameters for ihMT Brain Imaging at 1.5T. Magn. Reson. Med. 2015;73:2111–2121 doi: 10.1002/mrm.25330.

34. Girard OM, Callot V, Prevost VH, et al. Magnetization transfer from inhomogeneously broadened lines (ihMT): Improved imaging strategy for spinal cord applications: ihMT for Spinal Cord Applications. Magn. Reson. Med. 2017;77:581–591 doi: 10.1002/mrm.26134.

35. Mchinda S, Varma G, Prevost VH, et al. Whole brain inhomogeneous magnetization transfer (ihMT) imaging: Sensitivity enhancement within a steady-state gradient echo sequence: Whole Brain Inhomogeneous Magnetization Transfer (ihMT). Magn. Reson. Med. 2018;79:2607–2619 doi: 10.1002/mrm.26907.

36. Ercan E, Varma G, Mädler B, et al. Microstructural correlates of 3D steady-state inhomogeneous magnetization transfer (ihMT) in the human brain white matter assessed by myelin water imaging and diffusion tensor imaging: Ercan et al. Magn. Reson. Med. 2018;80:2402–2414 doi: 10.1002/mrm.27211.

37. Geeraert BL, Lebel RM, Lebel C. A multiparametric analysis of white matter maturation during late childhood and adolescence. Hum. Brain Mapp. 2019;40:4345–4356 doi: 10.1002/hbm.24706.

38. Munsch F, Varma G, Taso M, et al. Characterization of the cortical myeloarchitecture with inhomogeneous magnetization transfer imaging (ihMT). NeuroImage 2021;225:117442 doi: 10.1016/j.neuroimage.2020.117442.

39. Van Obberghen E, Mchinda S, le Troter A, et al. Evaluation of the Sensitivity of Inhomogeneous Magnetization Transfer (ihMT) MRI for Multiple Sclerosis. Am. J. Neuroradiol. 2018;39:634–641 doi: 10.3174/ajnr.A5563.

40. Rasoanandrianina H, Grapperon A-M, Taso M, et al. Region-specific impairment of the cervical spinal cord (SC) in amyotrophic lateral sclerosis: A preliminary study using SC templates and quantitative MRI (diffusion tensor imaging/inhomogeneous magnetization transfer). NMR Biomed. 2017;30:e3801 doi: 10.1002/nbm.3801.

41. Duhamel G, Prevost VH, Cayre M, et al. Validating the sensitivity of inhomogeneous magnetization transfer (ihMT) MRI to myelin with fluorescence microscopy. NeuroImage 2019;199:289–303 doi: 10.1016/j.neuroimage.2019.05.061.

42. Greer JM, Lees MB. Myelin proteolipid protein—the first 50 years. Int. J. Biochem. Cell Biol. 2002;34:211–215 doi: 10.1016/S1357-2725(01)00136-4.

43. Yarnykh VL. Actual flip-angle imaging in the pulsed steady state: A method for rapid three-dimensional mapping of the transmitted radiofrequency field. Magn. Reson. Med. 2007;57:192–200 doi: 10.1002/mrm.21120.

44. Nehrke K. On the steady-state properties of actual flip angle imaging (AFI): Steady-State Properties of AFI. Magn. Reson. Med. 2009;61:84–92 doi: 10.1002/mrm.21592.

45. Chang L-C, Koay CG, Basser PJ, Pierpaoli C. Linear least-squares method for unbiased estimation of T_1 from SPGR signals. Magn. Reson. Med. 2008;60:496–501 doi: 10.1002/mrm.21669.

46. Varma G, Girard OM, Mchinda S, et al. Low duty-cycle pulsed irradiation reduces magnetization transfer and increases the inhomogeneous magnetization transfer effect. J. Magn. Reson. 2018;296:60–71 doi: 10.1016/j.jmr.2018.08.004.

47. Varma G, Munsch F, Burns B, et al. Three-dimensional inhomogeneous magnetization transfer with rapid gradient-echo (3D ihMTRAGE) imaging. Magn. Reson. Med. 2020 doi: 10.1002/mrm.28324.

48. Helms G, Dathe H, Kallenberg K, Dechent P. High-resolution maps of magnetization transfer with inherent correction for RF inhomogeneity and T1 relaxation obtained from 3D FLASH MRI. Magn. Reson. Med. 2008;60:1396–1407 doi: 10.1002/mrm.21732.

49. Avants BB, Tustison NJ, Wu J, Cook PA, Gee JC. An Open Source Multivariate Framework for n-Tissue Segmentation with Evaluation on Public Data. Neuroinformatics 2011;9:381–400 doi: 10.1007/s12021-011-9109-y.

50. Steiger JH. Tests for Comparing Elements of a Correlation Matrix. Psychol. Bull. 1980;87:245–251.

51. Zou GY. Toward using confidence intervals to compare correlations. Psychol. Methods 2007;12:399–413 doi: 10.1037/1082-989X.12.4.399.

52. Diedenhofen B, Musch J. cocor: A Comprehensive Solution for the Statistical Comparison of Correlations Olivier J, editor. PLOS ONE 2015;10:e0121945 doi: 10.1371/journal.pone.0121945.

53. Taylor RE, Peterson RD. Comparison of spin–lattice relaxation measurements made in the presence of strong radiation damping. J. Mol. Struct. 2010;970:155–159 doi: 10.1016/j.molstruc.2010.02.071.

54. Varma G, Girard OM, Prevost VH, Grant AK, Duhamel G, Alsop DC. In vivo measurement of a new source of contrast, the dipolar relaxation time, T_{1D}, using a modified inhomogeneous magnetization transfer (ihMT) sequence: In Vivo Measurement of T_{1D} Using ihMT. Magn. Reson. Med. 2017;78:1362–1372 doi: 10.1002/mrm.26523.

55. Lundgaard I, Osório MJ, Kress B, Sanggaard S, Nedergaard M. White matter astrocytes in health and disease. Neuroscience 2014;0:161–173 doi: 10.1016/j.neuroscience.2013.10.050.

56. Helms G, Dathe H, Dechent P. Modeling the influence of TR and excitation flip angle on the magnetization transfer ratio (MTR) in human brain obtained from 3D spoiled gradient echo MRI. Magn. Reson. Med. 2010;64:177–185 doi: 10.1002/mrm.22379.

57. Rowley CD, Campbell JSW, Wu Z, et al. A model-based framework for correcting inhomogeneity effects in magnetization transfer saturation and inhomogeneous magnetization transfer saturation maps. Magn. Reson. Med. n/a doi: https://doi.org/10.1002/mrm.28831.

58. Kucharczyk W, Lenkinski RE, Kucharczyk J, Henkelman RM. The effect of phospholipid vesicles on the NMR relaxation of water: an explanation for the MR appearance of the neurohypophysis? AJNR Am. J. Neuroradiol. 1990;11:693–700.

59. Mäkelä HI, Gröhn OHJ, Kettunen MI, Kauppinen RA. Proton Exchange as a Relaxation Mechanism for T1 in the Rotating Frame in Native and Immobilized Protein Solutions. Biochem. Biophys. Res. Commun. 2001;289:813–818 doi: 10.1006/bbrc.2001.6058.

60. Yang W, Lee J, Leninger M, Windschuh J, Traaseth NJ, Jerschow A. Magnetization transfer in liposome and proteoliposome samples that mimic the protein and lipid composition of myelin. NMR Biomed. 2019:e4097 doi: 10.1002/nbm.4097.

61. Kucharczyk W, Macdonald PM, Stanisz GJ, Henkelman RM. Relaxivity and magnetization transfer of white matter lipids at MR imaging: importance of cerebrosides and pH. Radiology 1994;192:521–529 doi: 10.1148/radiology.192.2.8029426.

62. Salthouse TN. Luxol Fast Blue Arn: A New Solvent Azo Dye with Improved Staining Qualities for Myelin and Phospholipids. Stain Technol. 1962;37:313–316 doi: 10.3109/10520296209114492.

63. Lycette RM, Danforth WF, Koppel JL, Olwin JH. The Binding of Luxol Fast Blue Arn by Various Biological Lipids. Stain Technol. 1970;45:155–160 doi: 10.3109/10520297009067471.

64. Norton WT, Poduslo SE. Myelination in Rat Brain: Changes in Myelin Composition During Brain Maturation1. J. Neurochem. 1973;21:759–773 doi: https://doi.org/10.1111/j.1471-4159.1973.tb07520.x.

65. Ansell GB, Spanner S. Functional Metabolism of Brain Phospholipids. In: Smythies JR, Bradley RJ, editors. International Review of Neurobiology. Vol. 20. Academic Press; 1977. pp. 1–29. doi: 10.1016/S0074-7742(08)60649-2.

66. Spassky N, Olivier C, Cobos I, et al. The Early Steps of Oligodendrogenesis: Insights from the Study of the plp Lineage in the Brain of Chicks and Rodents. Dev. Neurosci. 2001;23:318–326 doi: 10.1159/000048715.

67. Bras BL, Chatzopoulou E, Heydon K, et al. Oligodendrocyte development in the embryonic brain: the contribution of the plp lineage. Int. J. Dev. Biol. 2003;49:209–220 doi: 10.1387/ijdb.041963bl.

68. Ferent J, Ruat M, Traiffort E. Investigation of the proteolipid protein promoter activity during demyelination and repair. Differentiation 2013;85:182–189 doi: 10.1016/j.diff.2013.05.002.

69. Sled JG, Pike GB. Quantitative Interpretation of Magnetization Transfer in Spoiled Gradient Echo MRI Sequences. J. Magn. Reson. 2000;145:24–36 doi: 10.1006/jmre.2000.2059.

70. Yu Y, Ramachandran PV, Wang MC. Shedding new light on lipid functions with CARS and SRS microscopy. Biochim. Biophys. Acta BBA - Mol. Cell Biol. Lipids 2014;1841:1120–1129 doi: 10.1016/j.bbalip.2014.02.003.

71. MacKay AL, Laule C. Magnetic Resonance of Myelin Water: An in vivo Marker for Myelin Zalc B, editor. Brain Plast. 2016;2:71–91 doi: 10.3233/BPL-160033.

72. Genain CP, Cannella B, Hauser SL, Raine CS. Identification of autoantibodies associated with myelin damage in multiple sclerosis. Nat. Med. 1999;5:170–175 doi: 10.1038/5532.

73. Hoffmann H. Violin Plot. https://www.mathworks.com/matlabcentral/fileexchange/45134-violin-plot. Published 2021. Accessed May 1, 2021.

Figure Captions

Main document

Table 1: Results of linear regression analyses between the MR metrics with the two microscopy references (MR signal = Y_intercept + Normalized plp-GFP Signal * slope and MR signal = Y_intercept + Normalized LFB Signal * slope). The values of the Y-intercept, slope and specificity are presented as estimated value ± standard error. Coefficients significantly different than zero (p-value < 0.05) are represented by the asterisk symbol (*). The specificity estimation of R_1 (†), for which the Y_intercept was corrected with the value of the metric in pure water measured at room temperature (53) might be slightly overestimated due to the higher in vivo temperature.

Table 2: Results of comparisons between pairs of overlapping correlation coefficients resulted from associations between the MR metrics with the two microscopy references. Plp-GFP (top) and LFB (bottom) are considered as the common variable. Significant p-values (p-value < 0.001 and p-value < 0.05) are accompanied by the asterisk symbol (*) and the 95% confidence intervals are reported. Pairs not indicated in this table were not significantly different.

Table 3: Results of comparisons between pairs of slopes (top) and intercepts (bottom) for ihMTsat (left) and ihMTR (right) when either plp-GFP (above the main diagonal) and LFB (below the main diagonal) was considered as the common variable.

Significant p-values (p-value < 0.001 and p-value < 0.05) are accompanied by the asterisk symbol (*).

Figure 1: Diagram summarizing the acquisition and processing steps from the raw images to the final quantitative and semi-quantitative metrics investigated in this study. The acquisition time for each MR sequence was: 4 mins 32 s for qMT; 9 mins 30 s for VFA; 1 min 59 s for AFI and 1 min 40 s for ihMTR. In the context of this study, the acquisition time necessary for the derivation of each metric was: 11 mins 29 s for R_1, 16 mins 01s for MPF, 8 mins 40 s for ihMTR ($\Delta t_{0.0}$) and 20 mins 9s for ihMTsat ($\Delta t_{0.0}$), 11 mins 20 s for ihMTR ($\Delta t_{0.8}$) and 22 mins 49 s for ihMTsat ($\Delta t_{0.8}$), 22 mins for ihMTR ($\Delta t_{3.2}$) and 33 mins 29 s for ihMTsat ($\Delta t_{3.2}$). The increasing time of ihMTR/ihMTsat as Δt is lengthened is due to an increasing number of averages of the raw MTw images. IhMTR and B_1 maps were generated by direct computation, whereas R_1, ihMTsat and MPF maps were generated via model fitting.

Figure 2: Templates of MR metrics and the corresponding fluorescence images at three levels of bregma (+0.7 mm, -1.0 mm, and -3.2 mm from bregma). The seven segmented ROIs are indicated by red arrows on the Plp-GFP and the T_2-weighted images.

Figure 3: Linear regression analysis between the LFB and plp-GFP normalized signals. One data point corresponds to the ROI average of one structure from one mouse.

Figure 4: Linear regression analyses between the MR metrics with the plp-GFP normalized signal (a - d) and the LFB normalized signal (e-h). One data point corresponds to the ROI average of one structure from one mouse.

Figure 5: Bivariate histograms for MPF and ihMTR $\Delta t_{0.0}$ (a, f, k), MPF and ihMTR $\Delta t_{0.8}$ (b, g, l), MPF and ihMTR $\Delta t_{3.2}$ (c, h, m), MPF and $\Delta t_{0.0}$-$\Delta t_{0.8}$ (d, i, n) for three different slices from the caudal to the rostral part of the brain (e, j, o). The bins were calculated with the Freedman–Diaconis rule.

Figure 6: Bivariate histograms for MPF and ihMTsat $\Delta t_{0.0}$ (a, f, k), MPF and ihMTsat $\Delta t_{0.8}$ (b, g, l), MPF and ihMTsat $\Delta t_{3.2}$ (c, h, m), MPF and $\Delta t_{0.0}$-$\Delta t_{0.8}$ (d, i, n) for three different slices from the caudal to the rostral part of the brain (e, j, o). The bins were calculated with the Freedman–Diaconis rule.

Figure 7: Plots of (a) r^2 correlation coefficients and (b) intercepts for the linear regression analyses between MPF and ihMT metrics on the 51 common template slices. The mean value of the distribution of each coefficient in all investigated slices is represented by a black line, and the median value by a red line. The wider sections of the violin plot represent a higher probability of the coefficients to take on the corresponding values represented on the x-axis. All the tested pairs were significantly different (p-value < 0.05), except for the comparisons accompanied by the corresponding non-significant p-values.

Supporting Information

Supporting Information Table S1: MR and microscopy quantifications in seven CNS structures (mCC – medial corpus callosum, INT – internal capsules and OPT – optical tract, TH – thalamus, CP – caudoputamen, CTX- cerebral cortex, HIP – hippocampal region). Mean absolute values and group standard deviations were calculated on the ROI averages of the six plp-GFP mice.

Supporting Information Table S2: Results of comparisons between pairs of correlation coefficients, slope, and Y_intercept estimated values resulted from associations of each MR metric with the two microscopy references. MR metrics are considered as the common variable. Significant p-values (p-value < 0.05) are accompanied by the asterisk symbol.

Supporting Information Figure S1: Example of linear regression analyses between MPF and ihMTR voxel-wise quantifications (MPF signal = Y_intercept + ihMTR signal * slope) on six different slices from the caudal to the rostral part of the brain (a to f). The corresponding $\Delta t_{0.0}$, $\Delta t_{0.8}$, MPF, and $\Delta t_{0.0}$ - $\Delta t_{0.8}$ images in the signal ranges [0%, 23%], [0%, 15%], [0%, 10%], and [0%, 10%] respectively, are illustrated.

Supporting Information Figure S2: Example of linear regression analyses between MPF and ihMTsat voxel-wise quantifications (MPF signal = Y_intercept + ihMTsat signal * slope) on six different slices from the caudal to the rostral part of the brain (a to f). The corresponding $\Delta t_{0.0}$, $\Delta t_{0.8}$, MPF, and $\Delta t_{0.0}$ - $\Delta t_{0.8}$ images in the signal ranges [0%, 23%], [0%, 15%], [0%, 10%], and [0%, 10%] respectively, are illustrated.

Table 1: Results of linear regression analyses between the MR metrics with the two microscopy references (MR signal = Y_intercept + Normalized plp-GFP Signal * slope and MR signal = Y_intercept + Normalized LFB Signal * slope). The values of the Y-intercept, slope and specificity are presented as estimated value ± standard error. Coefficients significantly different than zero (p-value < 0.05) are represented by the asterisk symbol (*). The specificity estimation of R_1 (†), for which the Y_intercept was corrected with the value of the metric in pure water measured at room temperature (53) might be slightly overestimated due to the higher in vivo temperature.

MR metrics		Normalized plp-GFP Signal				Normalized LFB Signal			
		r^2	Y_intercept	Slope (%)	Specificity (%)	r^2	Y_intercept	Slope (%)	Specificity (%)
R_1		* 0.67	* 0.4 ± 0.02	* 18.6 ± 2.4	† 65 ± 5	* 0.77	* 0.4 ± 0.01	* 16.0 ± 2.1	† 62 ± 4
MPF		* 0.83	* 3.8 ± 0.3	* 5.1 ± 0.4	58 ± 7	* 0.91	* 4.8 ± 0.2	* 4.4 ± 0.3	51 ± 5
ihMTR	$\Delta t_{0.0}$	* 0.85	* 5.7 ± 0.9	* 14.5 ± 1.2	73 ± 10	* 0.91	* 8.5 ± 0.7	* 12.6 ± 1.0	62 ± 7
	$\Delta t_{0.8}$	* 0.86	* 1.7 ± 0.6	* 10.9 ± 0.8	87 ± 12	* 0.88	* 4.3 ± 0.6	* 8.8 ± 0.8	70 ± 10
	$\Delta t_{3.2}$	* 0.79	0.3 ± 0.4	* 5.7 ± 0.5	95 ± 17	* 0.88	* 1.5 ± 0.3	* 5.0 ± 0.4	79 ± 11
	$\Delta t_{0.0}$ - $\Delta t_{0.8}$	* 0.46	* 4.0 ± 0.6	* 3.6 ± 0.7	49 ± 13	* 0.59	* 4.2 ± 0.5	* 3.8 ± 0.7	50 ± 12
ihMTsat	$\Delta t_{0.0}$	* 0.82	* 0.5 ± 0.2	* 3.3 ± 0.3	87 ± 14	* 0.91	* 1.1 ± 0.2	* 3.0 ± 0.2	75 ± 8
	$\Delta t_{0.8}$	* 0.84	0.04 ± 0.1	* 2.3 ± 0.2	98 ± 17	* 0.87	* 0.6 ± 0.1	* 1.9 ± 0.2	79 ± 13
	$\Delta t_{3.2}$	* 0.79	-0.04 ± 0.08	* 1.1 ± 0.1	104 ± 20	* 0.89	* 0.2 ± 0.06	* 1.0 ± 0.1	87 ± 15
	$\Delta t_{0.0}$ - $\Delta t_{0.8}$	* 0.60	* 0.5 ± 0.1	* 1.1 ± 0.2	71 ± 20	* 0.76	* 0.6 ± 0.1	* 1.1 ± 0.1	68 ± 10

Table 2: Results of comparisons between pairs of overlapping correlation coefficients resulted from associations between the MR metrics with the two microscopy references. Plp-GFP (top) and LFB (bottom) are considered as the common variable. Significant p-values (p-value < 0.001 and p-value < 0.05) are accompanied by the asterisk symbol (*) and the 95% confidence intervals are reported. Pairs not indicated in this table were not significantly different.

	plp-GFP as the common variable							
	ihMTsat			ihMTR				MPF
	$\Delta t_{0.0}$	$\Delta t_{0.8}$	$\Delta t_{3.2}$	$\Delta t_{0.0}$	$\Delta t_{0.8}$	$\Delta t_{3.2}$	$\Delta t_{0.0}$ - $\Delta t_{0.8}$	
ihMTsat ($\Delta t_{0.0}$ - $\Delta t_{0.8}$)	* < 0.001 [0.06, 0.3]	* 0.006 [0.04, 0.3]	* 0.031 [0.01, 0.3]	* < 0.001 [0.08, 0.3]	* 0.002 [0.05, 0.3]	* 0.031 [0.01, 0.3]	* 0.004 [-0.3, -0.02]	* 0.004 [-0.3, -0.05]
ihMTR ($\Delta t_{0.0}$ - $\Delta t_{0.8}$)	* < 0.001 [-0.5, -0.1]	* < 0.001 [-0.5, -0.09]	* 0.005 [-0.5, -0.06]	* < 0.001 [0.13, 0.48]	* < 0.001 [0.1, 0.5]	* 0.004 [0.06, 0.5]		* < 0.001 [-0.5, -0.01]
R_1	> 0.05	* 0.047 [0.001, 0.2]	> 0.05	* 0.029 [0.01, 0.2]	* 0.019 [0.01, 0.3]	> 0.05		* 0.045 [0.003, 0.2]
	LFB as the common variable							

	ihMTsat			ihMTR				MPF
	$\Delta t_{0.0}$	$\Delta t_{0.8}$	$\Delta t_{3.2}$	$\Delta t_{0.0}$	$\Delta t_{0.8}$	$\Delta t_{3.2}$	$\Delta t_{0.0}$ - $\Delta t_{0.8}$	
ihMTsat ($\Delta t_{0.0}$ - $\Delta t_{0.8}$)	* 0.007 [0.03, 0.2]	> 0.05		* 0.008 [0.03, 0.2]	> 0.05		* < 0.001 [-0.3, -0.04]	* 0.022 [-0.2, -0.01]
ihMTR ($\Delta t_{0.0}$ - $\Delta t_{0.8}$)	* < 0.001 [-0.4, -0.07]	* 0.017 [-0.4, -0.03]	* 0.007 [-0.4, -0.04]	* < 0.001 [0.08, 0.4]	* 0.016 [0.03, 0.4]	* 0.010 [0.04, 0.4]		* < 0.001 [-0.4, -0.05]
R_1	* 0.037 [0.005, 0.2]			> 0.05				* 0.037 [0.005, 0.2]

Table 3: Results of comparisons between pairs of slopes (top) and intercepts (bottom) for ihMTsat (left) and ihMTR (right) when either plp-GFP (above the main diagonal) and LFB (below the main diagonal) was considered as the common variable. Significant p-values (p-value < 0.001 and p-value < 0.05) are accompanied by the asterisk symbol (*).

Slope	ihMTsat				ihMTR			
	$\Delta t_{0.0}$	$\Delta t_{0.8}$	$\Delta t_{3.2}$	$\Delta t_{0.0}$ - $\Delta t_{0.8}$	$\Delta t_{0.0}$	$\Delta t_{0.8}$	$\Delta t_{3.2}$	$\Delta t_{0.0}$ - $\Delta t_{0.8}$
$\Delta t_{0.0}$		* 0.003	* < 0.001	* < 0.001		* 0.015	* < 0.001	* < 0.001

Intercept	ihMTsat				ihMTR			
	$\Delta t_{0.0}$	$\Delta t_{0.8}$	$\Delta t_{3.2}$	$\Delta t_{0.0}$ - $\Delta t_{0.8}$	$\Delta t_{0.0}$	$\Delta t_{0.8}$	$\Delta t_{3.2}$	$\Delta t_{0.0}$ - $\Delta t_{0.8}$
$\Delta t_{0.0}$		0.091	* 0.028	0.860		* < 0.001	* < 0.001	0.110
$\Delta t_{0.8}$	* 0.004		0.620	* 0.035	* < 0.001		0.071	* 0.012
$\Delta t_{3.2}$	* < 0.001	* 0.005		* 0.002	* < 0.001	* < 0.001		* < 0.001
$\Delta t_{0.0}$ - $\Delta t_{0.8}$	* 0.004	0.880	* 0.001		* < 0.001	0.910	* < 0.001	
$\Delta t_{0.8}$	* 0.003		* < 0.001	* < 0.001	* 0.004		* < 0.001	* < 0.001
$\Delta t_{3.2}$	* < 0.001	* < 0.001		0.880	* < 0.001	* < 0.001		* 0.029
$\Delta t_{0.0}$ - $\Delta t_{0.8}$	* < 0.001	* 0.001	0.540		* < 0.001	* < 0.001	0.180	

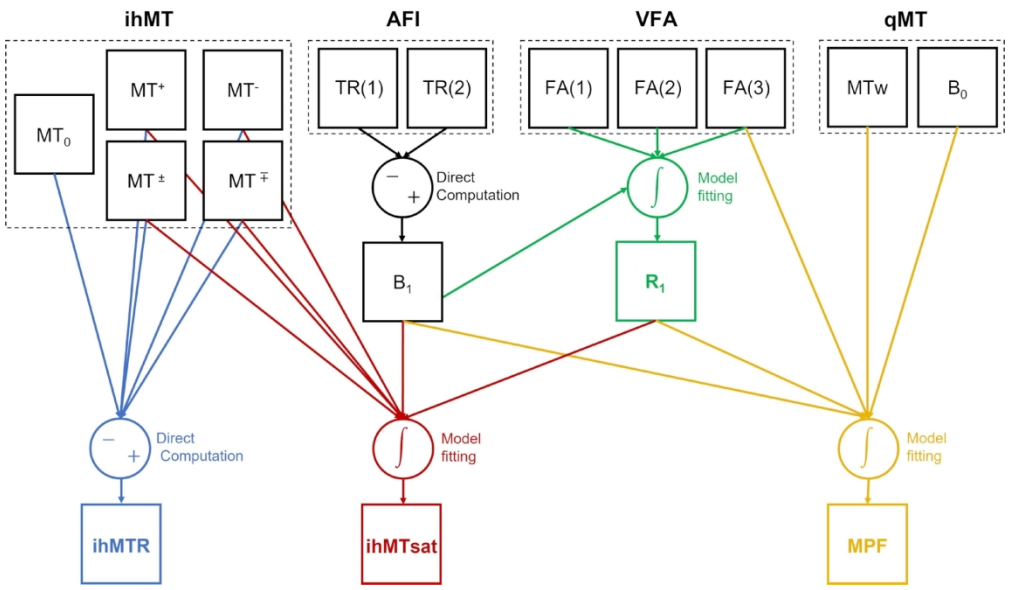

Figure 1: Diagram summarizing the acquisition and processing steps from the raw images to the final quantitative and semi-quantitative metrics investigated in this study. The acquisition time for each MR sequence was: 4 mins 32 s for qMT; 9 mins 30 s for VFA; 1 min 59 s for AFI and 1 min 40 s for ihMTR. In the context of this study, the acquisition time necessary for the derivation of each metric was: 11 mins 29 s for R_1, 16 mins 01 s for MPF, 8 mins 40 s for ihMTR ($\Delta t_{0.0}$) and 20 mins 9 s for ihMTsat ($\Delta t_{0.0}$), 11 mins 20 s for ihMTR ($\Delta t_{0.8}$) and 22 mins 49 s for ihMTsat ($\Delta t_{0.8}$), 22 mins for ihMTR ($\Delta t_{3.2}$) and 33 mins 29 s for ihMTsat ($\Delta t_{3.2}$). The increasing time of ihMTR/ihMTsat as Δt is lengthened is due to an increasing number of averages of the raw MT_w images. IhMTR and B_1 maps were generated by direct computation, whereas R_1, ihMTsat and MPF maps were generated via model fitting.

175x102mm (300 x 300 DPI)

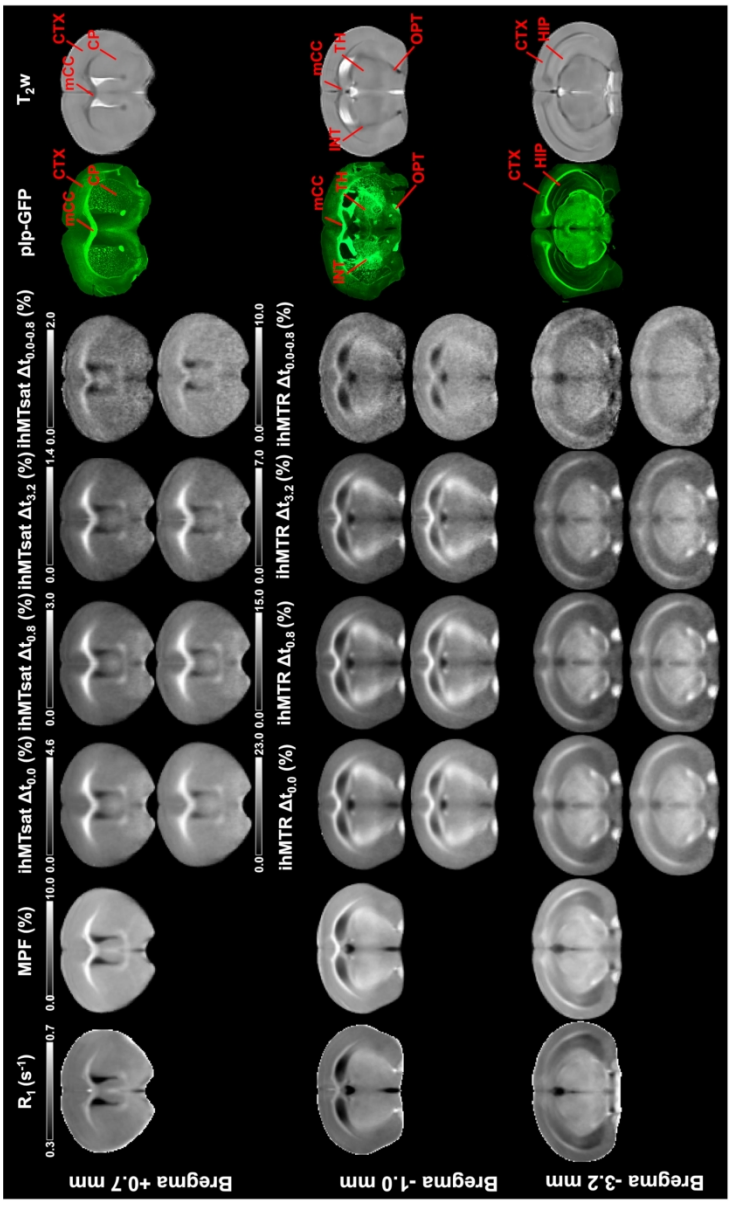

Figure 2: Templates of MR metrics and the corresponding fluorescence images at three levels of bregma (+ 0.7 mm, - 1.0 mm, and - 3.2 mm from bregma). The seven segmented ROIs are indicated by red arrows on the plp-GFP and the T_2-weighted images.

146x241mm (600 x 600 DPI)

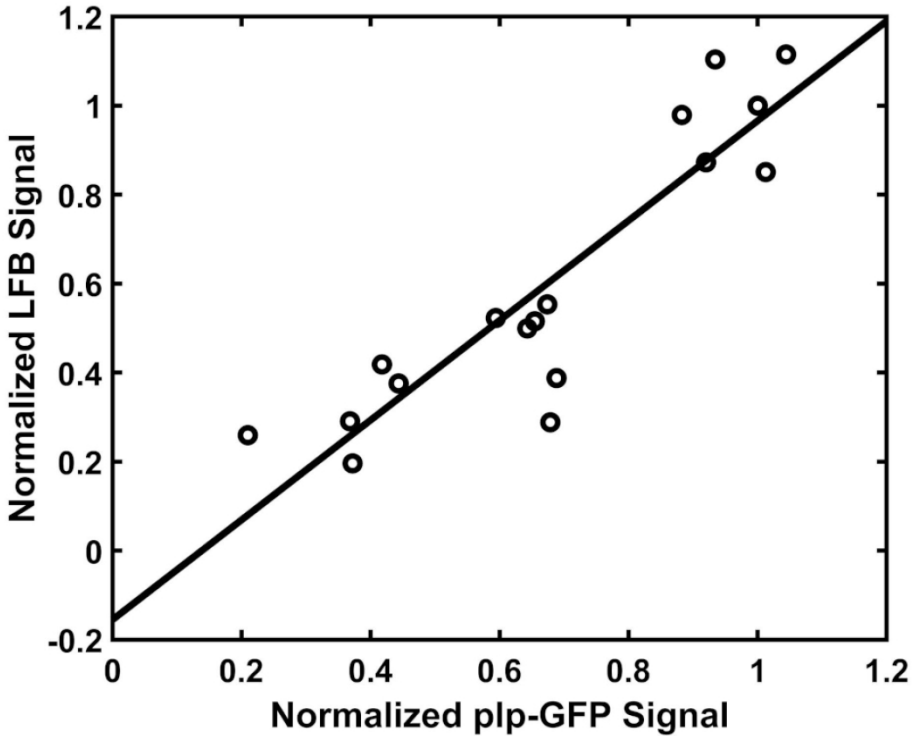

Figure 3: Linear regression analysis between the LFB and plp-GFP normalized signals.

86x67mm (600 x 600 DPI)

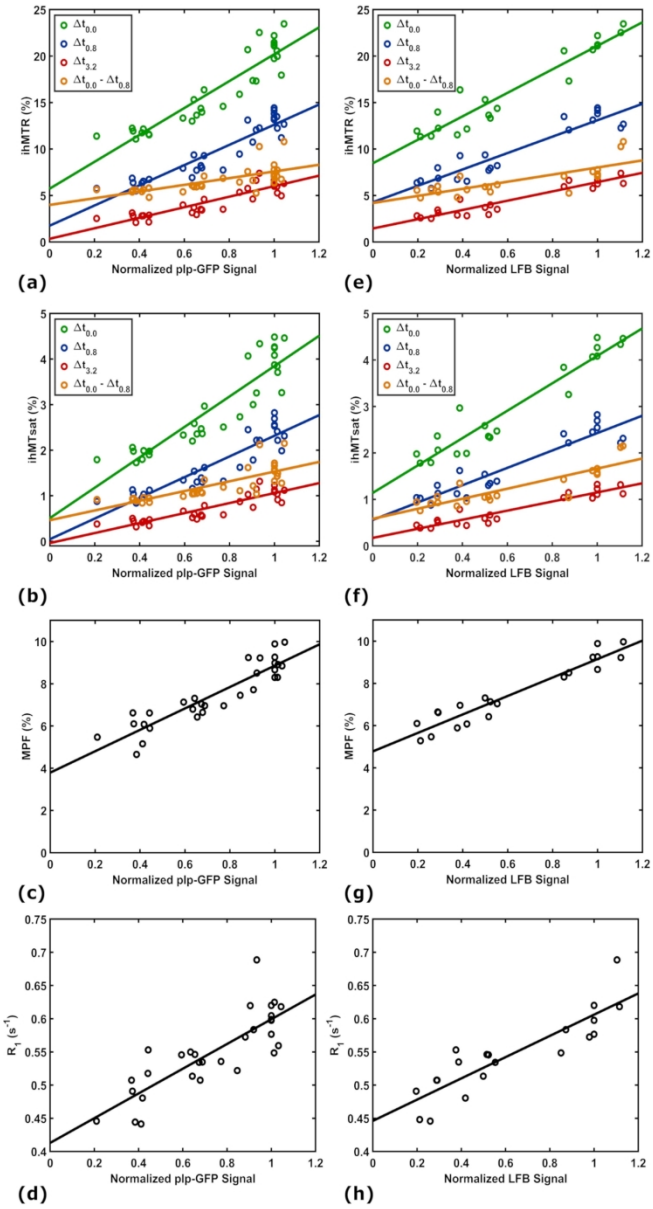

Figure 4: Linear regression analyses between the MR metrics with the plp-GFP normalized signal (a - d) and the LFB normalized signal (e-h). One data point corresponds to the ROI average of one structure from one mouse.

130x241mm (300 x 300 DPI)

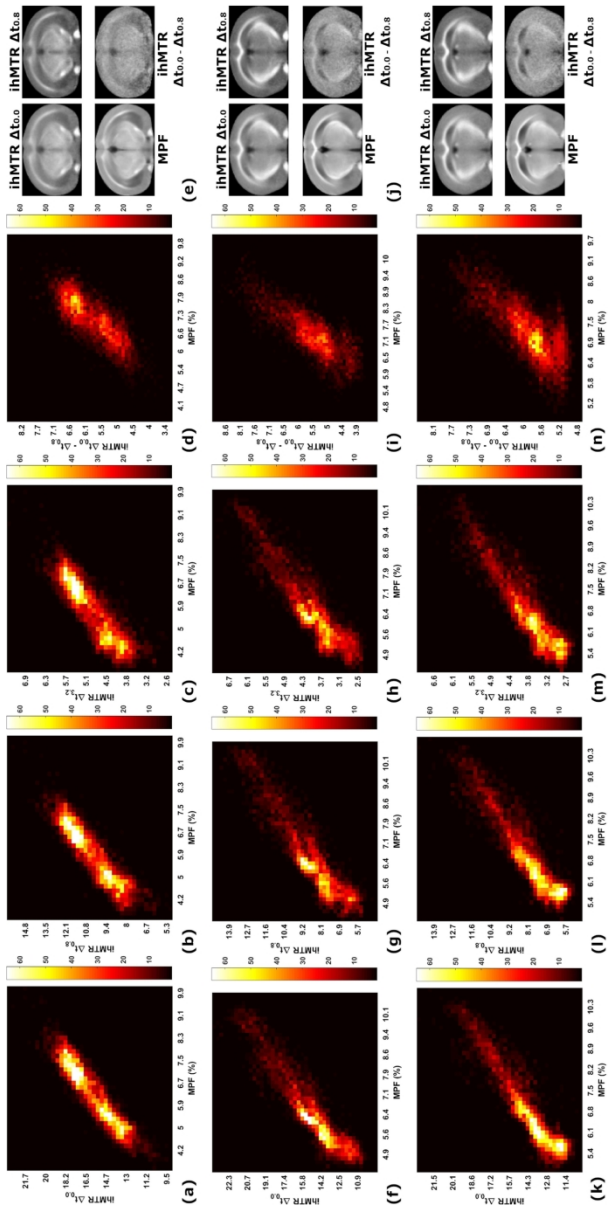

Figure 5: Bivariate histograms for MPF and ihMTR $\Delta t_{0.0}$ (a, f, k), MPF and ihMTR $\Delta t_{0.8}$ (b, g, l), MPF and ihMTR $\Delta t_{3.2}$ (c, h, m), MPF and $\Delta t_{0.0}$-$\Delta t_{0.8}$ (d, i, n) for three different slices from the caudal to the rostral part of the brain (e, j, o). The bins were calculated with the Freedman–Diaconis rule.

120x240mm (300 x 300 DPI)

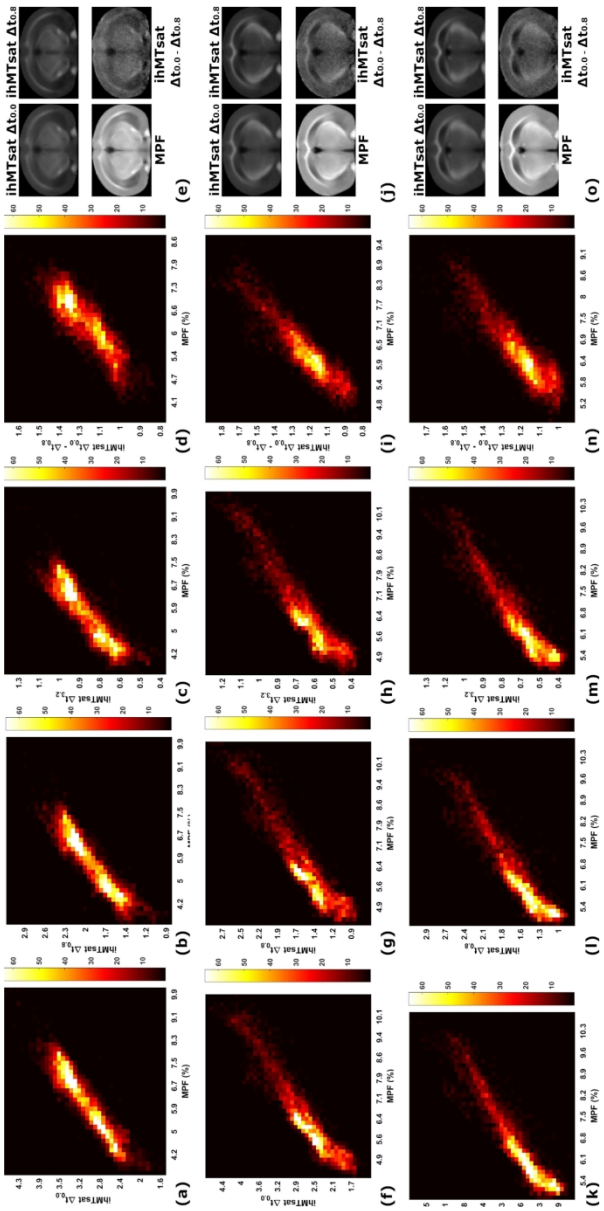

Figure 6: Bivariate histograms for MPF and ihMTsat $\Delta t_{0.0}$ (a, f, k), MPF and ihMTsat $\Delta t_{0.8}$ (b, g, l), MPF and ihMTsat $\Delta t_{3.2}$ (c, h, m), MPF and $\Delta t_{0.0}$-$\Delta t_{0.8}$ (d, i, n) for three different slices from the caudal to the rostral part of the brain (e, j, o). The bins were calculated with the Freedman–Diaconis rule.

119x240mm (300 x 300 DPI)

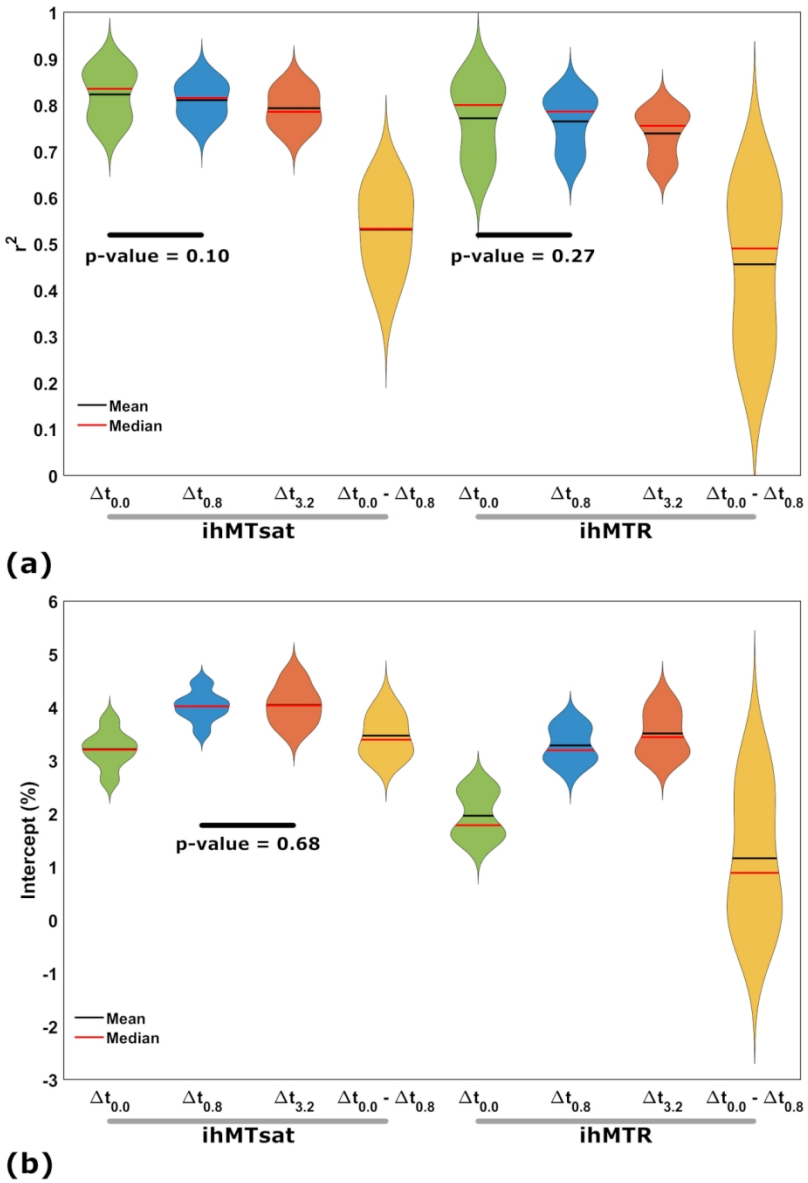

Figure 7: Plots of (a) r^2 correlation coefficients and (b) intercepts for the linear regression analyses between voxel-wise MPF and ihMT metrics on the 51 common template slices. The mean value of the distribution of each coefficient in all investigated slices is represented by a black line, and the median value by a red line. The wider sections of the violin plot (73) represent a higher probability of the coefficients to take on the corresponding values represented on the x-axis. All the tested pairs were significantly different ($p < 0.05$), except for the comparisons accompanied by the corresponding non-significant p-values.

165x241mm (600 x 600 DPI)